Materials Advances

ROYAL SOCIETY OF CHEMISTRY

PAPER

View Article Online
View Journal

Cite this: DOI: 10.1039/d5ma01116g

Protecting white Carrara marble with organophosphorus salts: a case study of ammonium hydrogen phenylphosphonate

Simone Murgia, [a] M. Carla Aragoni, [a] Gianfranco Carcangiu, [b] Simon J. Coles, [c] Stefano Columbu, [a] Guido Ennas, [a] Vito Lippolis, [a] Paola Meloni, *[de] Antonia Navarro Ezquerra, [f] James B. Orton, [c] Anna Pintus, [a] Enrico Podda, [ag] Daniel N. Rainer, [c] Domingo Gimeno Torrente *[h] and Massimiliano Arca *[a]

Ammonium hydrogen phenylphosphonate (**1**) was investigated as a novel agent for the protection and consolidation of carbonate stone substrates. Compound **1** quantitatively reacted with calcium carbonate to give calcium phenylphosphonate dihydrate (**2**), which was characterized by spectroscopic and microanalytical means and whose structure was solved using 3D electron diffraction. Compound **1** was applied to artificially weathered Statuario white Carrara marble mock-ups through immersion, brushing, and spraying techniques, and its effect on structural, hygric, and mechanical properties was evaluated by means of a comprehensive set of techniques, including X-ray diffraction, ultrasonic velocity measurements, colorimetry, porosimetry, and contact angle measurements. While the application of well-known diammonium hydrogen phosphate (DAP) on carbonate stones results in the deposition of non-stoichiometric hydroxyapatite (HAP), the treatment with compound **1** results in the formation of a thin, homogeneous coating of stoichiometric compound **2** that enhances cohesion, reduces porosity, and improves mechanical resistance, restoring the marble properties to near-pristine conditions. The treatment induces only minimal chromatic changes, making it a promising solution for the conservation of stone cultural heritage.

Received 29th September 2025,
Accepted 28th December 2025

DOI: 10.1039/d5ma01116g

rsc.li/materials-advances

Introduction

Marbles and limestones are among the most fascinating materials due to their historical use in sculpture and architecture. However, these natural calcareous stones are prone to deterioration caused by both natural and human-induced factors, such as climate conditions and exposure to pollutants.[1–6] A major cause of degradation is represented by the dissolution of calcite in water[7] (K_{sp} = 3.27 × 10^{-9} at 25 °C).[8] Acid rain in polluted urban environments increases the stone dissolution as well as the process of sulfation, while salt crystallization and particulate deposition further harm the carbonate structure, particularly in outdoor archaeological and heritage sites. Several organic[9–12] and inorganic compounds[13–17] have been studied for their ability to protect and/or consolidate carbonate matrices. Organic molecular compounds are generally easy to apply and provide immediate beneficial effects, but they are difficult to remove, have limited durability, and can cause irreversible changes to the original colour of marble.[13] In contrast, inorganic and organic salts are more compatible with the carbonate matrix of the stone, offering several advantages,

[a] Dipartimento di Scienze Chimiche e Geologiche, Università degli Studi di Cagliari, S. S. 554 Bivio per Sestu, 09042 Monserrato, Cagliari, Italy. E-mail: marca@unica.it
[b] Consiglio Nazionale Delle Ricerche (CNR), Istituto di Scienze dell'Atmosfera e del Clima (ISAC), UOS di Cagliari c/o Dipartimento di Fisica, Università degli Studi di Cagliari, S.S. 554 bivio per Sestu, 09042 Monserrato, Cagliari, Italy
[c] UK National Crystallography Service, School of Chemistry and Chemical Engineering, Faculty of Engineering and Physical Sciences, University of Southampton, SO17 1BJ, UK
[d] Dipartimento di Ingegneria Meccanica, Chimica e dei Materiali, Università degli Studi di Cagliari, via Marengo 2, 09123 Cagliari, Italy. E-mail: paola.meloni@unica.it
[e] Laboratorio Colle di Bonaria, Università degli Studi di Cagliari, Via Ravenna snc, 09125 Cagliari, Italy
[f] Departamento de Tecnología de la Arquitectura, EPSEB-UPC, Avda. Doctor Marañón, 44-50, 08028 Barcelona, Spain
[g] Centro Servizi di Ateneo per la Ricerca (CeSAR), Università degli Studi di Cagliari, S. S. 554 Bivio Sestu, 09042 Monserrato, CA, Italy
[h] Facultat de Ciències de la Terra, Universitat de Barcelona, c/Martí i Franquès s/n, 08028 Barcelona, Spain. E-mail: d.gimeno.torrente@gmail.com

including better solubility, environmental friendliness, low cost, and ease of preparation. For instance, the reinforcement of the carbonate microstructure can be achieved by applying $CaCO_3$, which can be deposited on the stone under appropriate conditions.[18] *In situ* carbonation can be facilitated by using suitable precursors such as barium and calcium hydroxides as well as nanolime.[1,19–22] Biomineralization represents a further approach for the deposition of a newly-formed calcium carbonate layer.[18,23–25] Since the mid-1980s, a promising approach involving the artificial coating of calcium oxalate (CaOx) using an appropriate precursor has been developed.[26] Ammonium oxalate, $(NH_4)_2(C_2O_4)$ (AmOx), reacts with calcium carbonate to afford calcium oxalate crystalline phases, $CaC_2O_4{\cdot}nH_2O$ (reaction (1)), in their monohydrate (whewellite; $n = 1$) and dihydrate (weddellite; $n = 2$) forms (solubility product $K_{sp} = 2.0 \times 10^{-9}$ and 3.8×10^{-9} at 25 °C, respectively).[27,28]

$$CaCO_3 + (NH_4)_2(C_2O_4) + (n-1)H_2O \rightarrow CaC_2O_4{\cdot}nH_2O + 2NH_3 + CO_2 \quad (1)$$

However, the resulting CaOx layer on treated marble samples is typically not thicker than a few tens of micrometres, depending also on the application method.[26,29] This limited thickness is due to several factors, including the low concentration of AmOx in aqueous solutions (maximum 0.4 mol L^{-1}, 5% w/w)[30] and the limited ability of water to penetrate deeply into the carbonate matrix, especially for poorly permeable stones, such as marble (generally showing a total porosity of $<0.5\%$). During the past decade, in an effort to overcome these intrinsic limitations of AmOx, several derivatives have been tested, including ammonium monoesters and monoamides (oxamates) of oxalic acid, which can form alternative insoluble calcium salts, such as in the case of ammonium oxamate[31] and *N*-phenyloxamate,[32] or behave as precursors of the oxalate anion,[33] as observed in the case of the treatments with ammonium methyl- and ethyl-oxalates[31,34] and *N*-(pyridin-2-yl)oxamate.[35]

Among inorganic salts, promising results have been obtained using diammonium hydrogen phosphate [DAP, $(NH_4)_2HPO_4$], a precursor of hydroxyapatite [HAP, $Ca_{10}(PO_4)_6(OH)_2$], as a consolidating agent for carbonate stones.[36,37] However, the treatment of calcium carbonate substrates with DAP results in the formation of non-stoichiometric products $Ca_{10}(PO_4,CO_3)_6(OH,CO_3)$, since carbonate ions can replace both OH^- and PO_4^{3-} anions.[38] Along with the main insoluble reaction products, other calcium phosphates, such as $Ca_8(HPO_4)_2(PO_4)_4{\cdot}5H_2O$[39] and $CaHPO_4{\cdot}2H_2O$ (brushite),[40,41] have been observed, and the latter is particularly undesirable[42] due to its higher solubility compared to calcite ($K_{sp} = 2.5 \times 10^{-7}$).[43,44] In addition, the formation of the pyrophosphate anion has been reported in systems with free Ca^{2+} ions.[45] The variability in the stoichiometry of the deposition on the surface can be related to the similar size of the anions, which are easily interchanged in the crystal lattice of the newly-formed depositions. In order to minimise the formation of byproducts, a variety of parameters have been tuned and tested, including the concentration of the DAP solution, the acidity of the solution,[46] the duration of the treatment,[36,47,48] the addition of external ions,[47,49] including exogenic Ca^{2+},[50] and the modulation of the polarity of the solution by using solvent mixtures.[51] Notably, different treatment methods, regardless of the nature of the adopted consolidant, can lead to different results and help modulate the effect of deposition on the stone surface.[52,53]

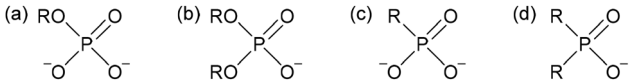

Chart 1 Organophosphorus anions: substituted phosphate (a) and (b), phosphonate (c), and phosphinate (d). R = alkyl or aryl substituents.

The synthetic functionalization of the phosphate anion offers a potential strategy to reduce the anion interchange, thereby achieving stoichiometric reproducible deposition, provided that the starting ammonium salt is soluble in water and the calcium salt is less soluble than calcite. Substituted organophosphorus anions include organophosphates, phosphonates, and phosphinates (Chart 1).[54]

In this work, the ammonium salt of the bulky hydrogen phenylphosphonate anion has been tested as a potential agent for the conservative treatment of carbonate stones, starting with the case study of Statuario white Carrara marble.

Results and discussion

Synthesis and characterization

Inorganic salts suitable for the treatment of calcium carbonate substrates must satisfy several criteria, including (i) a high solubility in water, allowing for a variety of treatment methods, ranging from immersion to spraying;[52,53,55] (ii) the resulting calcium derivative, acting as a surface protective and/or consolidating agent, must be poorly soluble, featuring a solubility product ideally comparable to that of calcite ($K_{sp} < 3.27 \times 10^{-9}$);[8] (iii) the reaction byproducts must be water soluble or volatile. In this context, ammonium is a suitable cation in salts containing substituted oxalate, oxamate and phosphate anions, since it releases ammonia and carbon dioxide when reacted with the carbonate anion (see reaction (1) for AmOx).

With the purpose of improving the performance and overcoming the limitations of DAP as an inorganic salt for the treatment of calcium carbonate substrates, we have turned to increase the hindrance of the anion, preserving the solubility of its ammonium salt, by passing from the phosphate to the phenylphosphonate anion (R = Ph in Chart 1c).

The reaction of phenylphosphonic acid with ammonium carbonate in water quantitatively affords ammonium hydrogen phenylphosphonate (AmHPP, **1**), according to reaction (2):

$$2H_2PhPO_3 + (NH_4)_2CO_3 \rightarrow 2(NH_4)(HPhPO_3) + CO_2 + H_2O \quad (2)$$

Compound **1**, isolated as white crystals, was characterised by microanalytical means (melting point determination and elemental analysis), spectroscopic methods (^1H, $^{13}C\{^1H\}$, and $^{31}P\{^1H\}$-NMR; FT-IR; UV-vis), and diffractometric techniques (Table S1 and Fig. S1–S6 in the SI). A DMSO-d_6 solution of

compound **1** displays a single signal in the $^{31}P\{^{1}H\}$-NMR spectrum at 8.40 ppm (Fig. S2 in the SI; 10.97 ppm in the solid-state CP-MAS $^{13}P\{^{1}H\}$-NMR spectrum, Fig. S6a in the SI), and the expected two multiplets, centred at 7.28 and 7.62 ppm, slightly downfield-shifted compared to the starting acid, in the ^{1}H-NMR spectrum (Fig. S1 in the SI). The powder X-ray diffractogram (PXRD) is in good agreement with the calculated PXRD pattern from the single-crystal X-ray diffraction (SC-XRD) data reported previously (Fig. S5 in the SI).[56,57] The lack of diffraction peaks of the starting acid in the PXRD diffractogram recorded for compound **1** is consistent with a complete conversion of the starting acid. The solubility of compound **1** in water was determined spectrophotometrically to be 0.93 mol L^{-1}, corresponding to 16% w/w. Thus, despite the functionalization of the phosphonate anion with a bulky phenyl group, the solubility of compound **1** remains sufficiently high to obtain relatively concentrated solutions ($\sim$0.9 mol L^{-1}).

Reactivity towards $CaCO_3$ powder

As mentioned above, one of the main drawbacks of using DAP as a consolidant is the formation, along with HAP, of other secondary phases on stone surfaces. This strongly depends on pH and can lead to metastable phases such as brushite and other soluble crystalline phases.[40,41] To assess the reactivity of ammonium phenylphosphonate towards carbonate-based stone surfaces, compound **1** and $CaCO_3$ powder were made to react in water in a 2 : 1 molar ratio under continuous stirring at ambient temperature (23 $\pm$ 2 °C) for 24 hours. The powder diffractograms collected on the filtered microcrystalline insoluble fraction (**2**) did not show the peaks of compound **1** (Fig. S5 in the SI). The CP-MAS $^{31}P\{^{1}H\}$-NMR spectrum recorded on compound **2** displayed a single signal at 13.28 ppm, being slightly upfield shifted compared to that of compound **1** (Fig. S6c in the SI). The CP-MAS $^{13}C\{^{1}H\}$ spectra (Fig. S6b and S6d in the SI) showed that the signals of the phenyl substituents in compound **2** are slightly upfield-shifted with respect to those of compound **1**. Thermogravimetric analysis (TGA) under nitrogen flow revealed a weight loss of humidity in the range of 30–90 °C (7.8%), a loss of crystallization water (7.4%) in the range of 90.5–193.8 °C, and a weight loss attributed to the organic fraction in the range of 193–769 °C (30.3%; Fig. S7 in the SI). The analysis of the differential scanning calorimetry (DSC) curve demonstrated that all the processes are endothermic (Fig. S8 in the SI). The elemental analysis carried out on the same solid excluded the presence of the ammonium cation and was consistent with compound **2** being calcium phenylphosphonate dihydrate, formed according to reaction (3):

$$(NH_4)(HPhPO_3) + CaCO_3 + H_2O \rightarrow Ca(PhPO_3)\cdot 2H_2O + NH_3 + CO_2 \quad (3)$$

3D electron diffraction (3D ED)

3D Electron diffraction (3D ED) has emerged as a powerful technique for the structural elucidation of small molecules, providing atomic resolution from crystals that are too small for conventional single-crystal X-ray diffraction (SC-XRD) analysis.[58,59] This is particularly relevant for materials where crystal growth is the main bottleneck due to the significant challenge of obtaining crystals of sufficient sizes for traditional X-ray crystallography. 3D ED demonstrated its potential in fields such as drug discovery, metal–organic frameworks, and materials science.[60] In this context, materials with extremely low solubility product values pose a significant challenge for crystallization, and 3D ED offers a valuable alternative for their structural characterization.

The very low solubility of compound **2** prevented the growth of single-crystals suitable for SC-XRD analysis. However, the solid directly isolated from the reaction of compound **1** and $CaCO_3$ powder (see above) proved to be suitable for crystal structure determination using 3D ED. This is, to the best of our knowledge, the first example of a structural characterization carried out by 3D ED in the context of cultural heritage conservation, highlighting the application of this sough-after technique for the study of materials relevant to this field.[61] According to 3D ED analysis, compound **2**, formulated as $Ca(PhPO_3)\cdot 2H_2O$, in perfect agreement with elemental analysis and TGA measurements (see above), crystallizes in the orthorhombic space group *Pbca*. The asymmetric unit comprises a single calcium(II) ion, a phenylphosphonato dianion, and two independent water molecules, one of which is coordinated to the calcium ion (Fig. S9 and Table S2 in the SI). The Ca^{2+} ion exhibits a coordination number 7, with five positions occupied by symmetry-related phenylphosphonate oxygen atoms (O1–O3) and the remaining two by water molecules (O4; Fig. 1). The crystal packing consists of a 2D-layered network in which calcium nodes are interconnected by phenylphosphonate moieties and water molecules, with the phenyl rings protruding out of the layers, which extend parallel to the *bc* plane (Fig. 2).

Water molecules (O5, Fig. S9 in the SI) fill the interlayer spaces left by the partially interdigitated phenyl rings (Fig. 2a). In Fig. 2b, the predicted crystal morphology obtained using the Bravais Friedel Donnay Harker (BFDH) method implemented in Mercury is depicted.[62] Finally, the structure model was refined against 3D ED data using the Rietveld method (Fig. S10 in the SI), confirming that compound **2** was the only crystalline phase present.

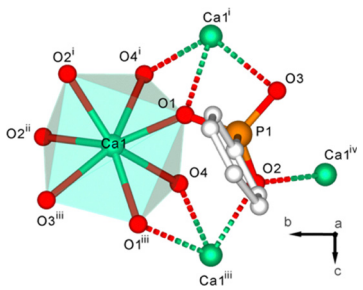

Fig. 1 View of the crystal structure of compound **2** along the *a*-axis. Symmetry codes: ^{i} = +*x*, 3/2 − *y*, −1/2 + *z*; ^{ii} = 1 − *x*, 1/2 + *y*, 3/2 − *z*; ^{iii} = +*x*, 3/2 − *y*, 1/2 + *z*; ^{iv} = 1 − *x*, −1/2 + *y*, 3/2 − *z*.

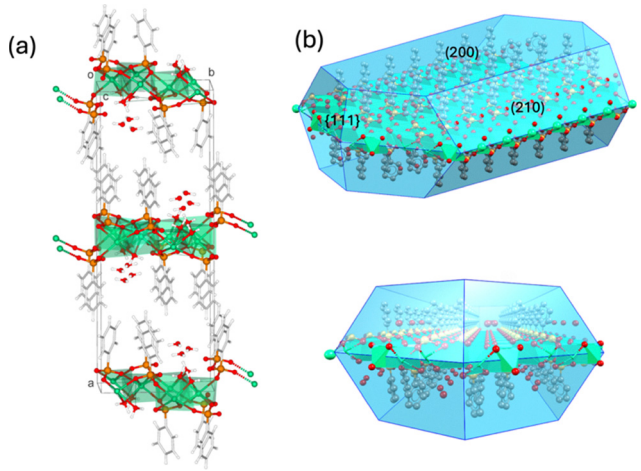

Fig. 2 (a) Crystal packing seen along the *c*-axis; (b) predicted crystal morphology of compound **2**.

Assays with Statuario white Carrara marble fragments

White marble specimens (prisms 2.0 × 2.0 × 8.0 cm: cubes 2.0 × 2.0 × 2.0 cm; fragments ∼1 cm^3) were artificially weathered by a slow heating process (from r.t. to 300 °C, 2.3 °C min^{-1}), followed by a static heating (300 °C, 5 h), and subsequent cooling to r.t. (4.6 °C min^{-1}; Fig. S11 in the SI). Due to the intrinsic anisotropy of the structure of marble, the treatment was applied twice, by turning over the stone mock-ups before the second application. The degree of weathering was evaluated by measuring the ultrasonic speed within the stone sample, which was found to decrease from 2.8 km s^{-1} in the pristine specimens to 1.2 km s^{-1} in the weathered specimens. The weathering process therefore led the samples to a condition of severe risk of structural breakdown (class IV according to Köhler classification),[63,64] without altering the mineralogic composition of the samples. Overall, the thermal cycle induced a general degradation of the dynamic and structural bulk and surface features as compared to the intact sample reminiscent of that displayed by naturally weathered marble (Table 1).[65] Accordingly, the scanning electron microscopy (SEM) analysis on the weathered marble samples revealed microcracks around the edges of the specimens and a detachment of boundary calcite grains (Fig. S12 in the SI).

The thermally weathered samples were treated with a 5.0% w/w (0.30 mol L^{-1}) aqueous solution of compound **1** (pH = 5.0 at r.t.; conductivity = 15.3 ± 0.1 mS cm^{-1}) using different application techniques: (i) 24 h immersion in a static bath, following the protocol previously adopted for oxalate and oxamate derivatives;[31–35] (ii) brushing (10 brushstrokes); and (iii) spraying using a pressure nebulizer up to rejection (from a controlled distance of 20 cm and a flow rate of 16.4(8) mL min^{-1}). The amount of deposited compound **2** was evaluated on three of the largest mock-ups (4.5 × 4.5 × 2.0 cm), weighed before and after the application of each consolidating treatment. The spraying and brushing techniques were proved to be the most effective (3.1(5) and 3(1) mg cm^{-2}, respectively), followed by the immersion treatment (1.3(4) mg cm^{-2}).

The marble specimens were analysed before and after the treatments (Table 1 and Table S1, Fig. S12–S18 in SI) by means of a comprehensive set of techniques, namely powder X-ray diffraction (PXRD), colorimetry, surface roughness determination, ultrasonic propagation, water saturation measurements (including under pressure), Helium pycnometry, mercury intrusion porosimetry (MIP), shore scale hardness (C and D), pull-off test, liquid and vapour water permeability, capillary uptake, determination of drying properties, optical microscopy (OM) and SEM. Helium pycnometry and MIP require small irregular fragments (∼1 cm^3, ∼3 g), and samples that were not suitable for the brushing and spraying treatments.

SEM images of the marble samples treated by immersion revealed a uniform coating of small crystals a few micrometers in size, distributed across the surfaces and localized along the fractures and grain boundaries (Fig. 3). SEM and OM images of sections of the treated samples clearly showed a coating 10–15 μm thick (Fig. 3 and Fig. S13 in the SI). The fine coating acts as a cement between disjointed grains with an efficient consolidation, reaching a penetration depth of a few hundred of micrometers. PXRD analyses carried out directly on the treated surfaces confirmed that compound **2** is the only crystalline component of the coating (Fig. S14 in the SI).

Since the mass of compound **2** penetrated in the marble texture is small (lower than 0.1% with respect to calcite), SEM-EDS measurements for determining the phosphorus content could not be used to evaluate the penetration depth, which was estimated visually by OM. Visual analysis of the surfaces and cross-section of the mock-ups treated by brushing and spraying showed coating thicknesses of about 20 and 15 μm, and penetration depths as large as about 150 and 270 μm, respectively (Fig. S15 in the SI).

Since thermal weathering did not induce a complex internal porous structure, these results suggest that all the treatment protocols led to the deposition of consolidating phases, even with the reduced porosity of the marble mock-ups used in this study. Therefore, better results can be expected for the treatments of stone featuring a higher porosity, such as real marble artifacts from authentic restoration sites, or different lithotypes, for example biomicrites[31–34] and carbonate sandstones.

A comparison of the surface roughness measured on the same samples before and after the weathering and after the consolidation treatments showed that the mean roughness depth R_z increased by up to +36% as a result of the weathering thermal cycle. However, R_z decreased sensibly after all the treatments, restoring the roughness approximately to the value of the pristine samples (Table 1). In addition, the treated samples exhibited an improved cohesion, as evidenced by a marked increase in the ultrasonic velocity v_{uts} and the dynamic elastic index E_d, partially restoring, and in the case of the brush application, even improving the properties of the pristine marble samples (Table 1). Accordingly, in the case of the immersion treatment, the average pore size of treated marble, determined by MIP,[66,67] was reduced as compared to both untreated specimens (Fig. S16 in the SI). Notably, the increased porosity determined by MIP after the treatments can be

Table 1 Macroscopic properties of pristine (PR), weathered (TW), and treated (TR) marble samples and relative variations (%) of TR samples with respect to PR ($\Delta\%_{Improve}$) and TW ($\Delta\%_{Restore}$) samples. Characterization: ultrasonic propagation time, t_{uts}; ultrasonic propagation speed, v_{uts}; Young's elastic modulus, E_d; skeletal density from water saturation, $\rho_{skeletal\,H_2O}$; skeletal density from water saturation under pressure, $\rho_{skeletal\,H_2O\,vac.}$; bulk density from water saturation, $\rho_{bulk\,H_2O}$; bulk density from water saturation under pressure, $\rho_{bulk\,H_2O\,vac.}$; compact index, I_c%; water open porosity, Φ_{H_2O}%; water open porosity under pressure, $\Phi_{H_2O\,vac}$%; shore scale hardness *C*, HC; shore scale hardness *D*, HD; tensile strength, f_h; CIELAB colour space coordinates, L^*, a^* and b^*; chromatic index, *C*; white index, WI; colour difference ΔE; arithmetical mean roughness value, R_a; mean roughness depth, R_z; root mean square roughness, R_q; contact angle, ϑ_c, measured after 2, 30, or 60 s; drying index, DI; capillary uptake coefficient, CA; liquid water permeability, *w*; vapor water resistance, μ

Property	PR	TW	$\Delta\%_{Weather}$	Immersion	$\Delta\%_{Improve}$	$\Delta\%_{Restore}$	Brushing	$\Delta\%_{Improve}$	$\Delta\%_{Restore}$	Spraying	$\Delta\%_{Improve}$	$\Delta\%_{Restore}$
Dynamics												
t_{uts} (μs)	29.0 ± 0.1	68.9 ± 0.1	+138	38.2 ± 0.1	+31.7	−44.6	26.0 ± 0.1	−10.3	−62.3	37.0 ± 0.1	+27.6	−46.3
v_{uts} (km s^{-1})	2.8 ± 0.2	1.2 ± 0.1	−60	2.1 ± 0.1	−25	+75	3.1 ± 0.2	−11	+160	2.2 ± 0.2	−21	+83
E_d (MN m^{-2})	14.1 ± 0.5	2.41 ± 0.04	−82.9	7.7 ± 0.2	−45.4	+219	16.5 ± 0.6	−17.0	+585	8.2 ± 0.2	−41.8	+240
Structure												
$\rho_{skeletal\,H_2O}$ (g cm^{-3})	2.724(2)	2.729(6)	+0.18	2.719(2)	−0.18	−0.37	2.70(2)	−0.88	−1.1	2.708(4)	−0.59	−0.77
$\rho_{skeletal\,H_2O\,vac.}$ (g cm^{-3})	2.70(1)	2.689(2)	−0.41	2.70(1)	0.00	+0.41	2.70(1)	0.00	+0.41	2.70(1)	0.00	+0.41
$\rho_{bulk\,H_2O}$ (g cm^{-3})	2.705(3)	2.724(2)	+0.70	2.677(3)	−1.04	−1.73	2.68(2)	−0.92	−1.62	2.664(1)	−1.52	−2.20
$\rho_{bulk\,H_2O\,vac.}$ (g cm^{-3})	2.67(1)	2.637(3)	−1.24	2.639(6)	−1.16	+0.08	2.637(5)	−1.24	0.00	2.64(1)	−1.12	+0.11
I_c%	99.3	98.2	−1.07	98.5	−0.85	+0.22	99.4	+0.08	+1.16	98.4	−0.92	+0.15
Φ_{H_2O}%	0.54(4)	1.6(1)	+200	1.4(2)	+160	−12	0.6(1)	+11	−62	0.9(1)	+70	−44
$\Phi_{H_2O\,vac}$%	1.2(1)	2.0(1)	+67	2.3(2)	+92	+15	2.2(1)	+83	+10	2.4(1)	+100	+20
HC	93.7(8)	85(2)	−9.28	92(1)	−1.8	+8.2	94(2)	+0.32	+11	95(2)	+1.4	+12
HD	87(1)	75(1)	−14	86(2)	−1.1	+15	90(2)	+3.5	+20	92.3(8)	+6.09	+23.1
f_h (N mm^{-2})	0.76 ± 0.02	0.46 ± 0.02	−39	0.66 ± 0.02	−13	+44	0.85 ± 0.02	+12	+85	0.80 ± 0.02	+5.3	+74
Colorimetry												
L^*	92.72	94.50	—	94.53	—	—	93.51	—	—	94.40	—	—
a^*	−0.31	−0.13	—	−0.18	—	—	0.06	—	—	−0.28	—	—
b^*	−0.59	0.60	—	0.28	—	—	2.46	—	—	0.46	—	—
C	0.67	1.04	—	0.33	—	—	2.50	—	—	0.54	—	—
$WI_{CIELAB76}$	85.05	79.41	—	85.23	—	—	72.75	—	—	84.12	—	—
$\Delta E_{CIE1976}$	—	—	2.15	—	2.01	0.32	—	3.17	2.15	—	2.15	1.06
$\Delta E_{CIE2000}$	—	—	1.62	—	1.41	0.32	—	3.01	1.87	—	1.62	1.07
Roughness												
R_a (μm)	5.0(3)	6.4(5)	+28	5.7(6)	+14	−11	5.5(3)	+10.00	−14.06	6.0(5)	+20	−6.3
R_z (μm)	45(5)	61(6)	+36	48(3)	+6.7	−21	47(4)	+4.44	−22.95	40(5)	−11	−34
R_q (μm)	6.3(7)	8.6(6)	+36	8(1)	+30	−7	7.0(3)	+11.11	−18.60	7.7(7)	+20	−10
Contact angle												
ϑ_c 2 s_{left} (°)	44(12)	9(6)	—	49(14)	—	—	58(5)	—	—	92(10)	—	—
ϑ_c 2 s_{right} (°)	39(5)	11(7)	—	50(13)	—	—	57(3)	—	—	96(16)	—	—
ϑ_c 30 s_{left} (°)	32(12)	—	—	40(10)	—	—	56(6)	—	—	66(1)	—	—
ϑ_c 30 s_{right} (°)	31(8)	—	—	45(10)	—	—	53(5)	—	—	64.3(1)	—	—
ϑ_c 60 s_{left} (°)	32(12)	—	—	37(8)	—	—	51(7)	—	—	60(3)	—	—
ϑ_c 60 s_{right} (°)	27(8)	—	—	41(10)	—	—	51(4)	—	—	57(2)	—	—
Hydric												
DI (%h^{-1})	297(32)	66(1)	−78	66(2)	−77.78	0.0	65(2)	−78.11	−1.5	64.9(4)	−78.1	−1.67
CA (kg m^{-2} h$^{-1/2}$)	0.14(1)	2.81(4)	+1900	1.41(1)	+907.14	−50.0	0.96(7)	+585.71	−66	0.92(4)	+560	−67
w (kg m^{-2} h$^{-1/2}$)	0.03(1)	0.10(2)	+200	0.05(1)	+66.67	−50	0.09(2)	+200.00	−10	0.06(1)	+100	−40
μ	69(4)	27(4)	−61	68(2)	−1.45	+150	70(3)	+1.45	+160	105(5)	+52.1	+300

tentatively attributed to a novel secondary porosity, as previously observed in the case of the treatment with ammonium *N*-phenyloxamate.[32] This can be ascribed to the newly-deposited phase, resulting in a new unimodal pore distribution, with an average size of approximately 1.5 μm. This addition did not significantly modify the average pore size of the treated mock-ups with respect to the pristine marble, ensuring the preservation of the natural porosity of the stone. Contact angle measurements clearly showed the effects of surface degradation caused by weathering and subsequent restoration following treatment with compound **1**.

Untreated marble displayed an average contact angle of water ϑ_C^{2s} = 44(12)° measured 2 s after the droplet deposition (Table 1 and Fig. 4). This angle was remarkably lower after a longer delay. Weathered samples exhibited a minimal contact angle ϑ_C^{2s} (about 10°), and a measurement with a delay larger than 2 s was not possible. Samples treated by immersion showed a ϑ_C^{2s} value restored to about 50°. While this value

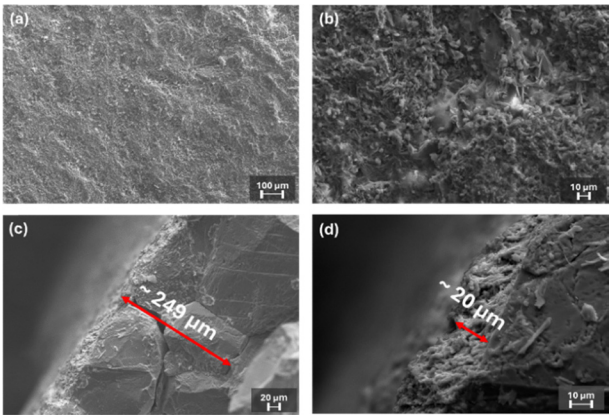

Fig. 3 SEM images of weathered Carrara marble treated by immersion with a 5% w/w solution of compound **1**: (a) and (b) mock-up surface, (c) cross-section, penetration width, and (d) cross-section, film width.

was well below 90°, a conventional threshold between hydrophilic and hydrophobic behaviour, it indicates a lower wettability of the treated marble surface compared to the pristine non-weathered specimens. It is worth noting that these results obtained on specimens treated by immersion are very close to those reported for marble samples treated by brushing with DAP and nanolime (ϑ_C^{5s} = 55 ± 1 and 49 ± 1°, respectively).[68,69]

When the solution of compound **1** was applied by brushing and spraying, larger values of contact angle were obtained (Table 1 and Fig. 4), reaching, in the case of the latter, the hydrophobization of the surface, thus potentially increasing the resistance towards chemical and biological agents. These results suggest that the brushing and spraying application methods produce a more homogeneous covering layer as compared to immersion.

The effects induced by the consolidation treatment were further elucidated by investigating the variation in the water transport properties. The increased rugosity and microfractures between the calcite grains induced by the thermal weathering

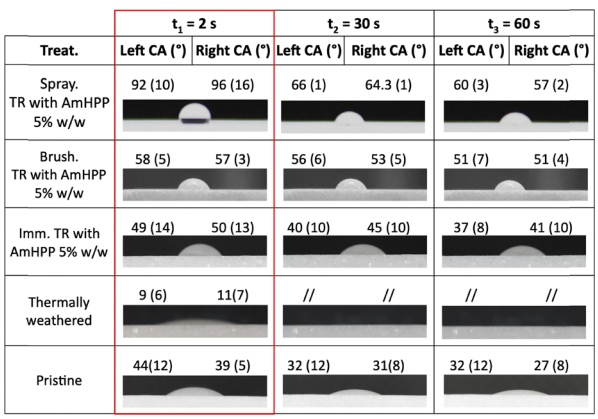

Fig. 4 Contact angle measurements performed on both untreated and treated stone mock-ups. For each treatment, three analyses are shown at 2, 30 and 60 s after the deposition of the water drop.

(Fig. S12 in the SI) are reflected in an increase in both the speed and the amount of water sorbed during the capillary uptake. On the other hand, after the treatments, a slight decrease in the water capillary uptake speed was observed, as shown by the capillary absorption coefficient CA. The drying curves showed no significant difference after the application of the consolidant (Table 1 and Fig. S17 in the SI). This can be tentatively attributed to the new micrometric secondary porosity obtained with the deposition of calcium phenylphosphonate dihydrate, evidenced by MIP measurements (see above). The indices derived from the sorption curves were compared with the results of a water saturation test performed under pressure (Table 1). The increase in the material porosity after the weathering process confirms the results obtained from MIP measurements, while the recovery of the skeletal density to a value comparable to that of the pristine marble ensures the preservation of the normal density of calcite (2.71 g cm^{-3}).[70]

To better understand the effect of the new deposited phases on the material permeability, the liquid water permeability index and vapour water permeability resistance were determined for all the mock-ups, before and after the artificial weathering and after the consolidating treatments (Table 1). The indices showed an increase in water permeability after the weathering, which was reduced following the application of compound **1**, resulting in the formation of a coating of compound **2**.

The variations in the chromatic indices $\Delta E_{CIELAB1976}$ and $\Delta E_{CIELAB2000}$ between the treated and the original untreated samples were evaluated, obtaining values well below the threshold value of 3 (Table 1). This indicates that the treatment did not produce significant colour changes perceptible to the naked eye (Fig. S18 in the SI).[40,71,72]

Finally, the mechanical resistance of the deposited layer of compound **2** was tested by means of surface durimetry (shore C and D scale), followed by a measure of the cohesion of Carrara marble with a pull-off test (determination of the tensile strength, f_h; Table 1). The results indicated a substantial improvement in the mechanical resistance of the material following the consolidation treatment, with immersion treatment almost restoring the property of the pristine marble, while the brushing and spraying applications ensure even better consolidating effects, as confirmed by the higher values of hardness and tensile strength.

Accelerated aging

Mock-ups treated with a 5.0% w/w (0.3 mol L^{-1}) solution of compound **2** were subjected to different accelerated aging tests. Thermal shock (T–S) tests were carried out according to the EN 140666:2014 standard method (Fig. S19 and Table S3 in the SI).[73] Subsequently, freeze–thaw (F–T) resistance experiments were carried out (Fig. S19 and Table S3 in the SI), on another set of mock-ups, as specified in EN 12371:2010.[74] Both methodologies involve a consequent temporary change in the grain size dimension, but in the case of F–T tests the formation of ice inside the fractures or pores of the material could be

observed. The outcome of the two thermal shock experiments was monitored with a preliminary visual inspection and determination of the Young's elastic modulus by means of ultrasonic propagation speed. For both treatments, only very minor damages of the mock-ups were detected (score 1 according to the F–T standard),[74] which did not compromise the integrity of the specimens (Fig. S19 in the SI). The loss in elastic modulus (Table S3 in the SI) in the case of the T–S tests was significant only for the pristine and thermally weathered specimens. In contrast, in the case of F–T a significant decrease in the elastic modulus was observed only for the pristine material, suggesting that the fractures of the thermally weathered specimens were already wide enough not to induce an internal compression of the material during the formation of ice. In general, whatever the treatment method, the mock-ups consolidated with compound **1** showed a Young's elastic modulus always higher than the that of thermally weathered specimens, and in most cases even higher than pristine specimens, after both T–S and F–T tests.

Moreover, the resistance to acid rains was tested following the same methodology reported in the literature for mock-ups treated with DAP.[7,49,75] While both HNO_3 and HCl can be used for this test, the former was preferred, as the latter causes the lowest ion exchange with calcium phosphates/phosphonate salts (*e.g.* HAP).[76] The mock-ups (Fig. S20 in the SI) were visually inspected by SEM before and after the treatments (Fig. S21 and S22 in the SI, respectively), consisting of keeping the samples immersed for 24 h in a solution at pH = 5 (average harsher conditions of pH in European rains).[49] The effect of acid treatment was also evaluated by ultrasonic propagation speed measurement, colourimetry, rugosimetry, and superficial hardness (Table S4 in the SI). In the case of the pristine and the thermally weathered mock-ups, SEM imaging showed the effect of acid washing on carbonate rocks, with the clear dissolution of the material (Fig. S23a and b in the SI). Accordingly, the acid treatment had a flattening effect on the surface of pristine specimens, as denoted by average rugosity.

In the case of the materials treated with compound **1**, the deposition of compound **2** acted as a passivating/sacrificial layer and was partially removed instead of calcite, showing a similar behaviour to what it was reported for stone samples treated with DAP.[75] When the covering layer was locally removed with the detachment of a crystallite, the material was protected by penetrated compound **2** (Fig. S23c in the SI), unless the acid attacked directly the exposed calcite (Fig. S23d in the SI). Since no fractures were formed during the treatment, the physical effect of the acidic attack was limited to the surface (Table S4 in the SI), and no significant changes in ultrasonic propagation speed, Young's elastic modulus, and superficial hardness were detected. Oppositely, the colour was generally slightly affected by the acidic treatment, with a decrease in the white index for all the specimens, visually detectable ($\Delta E_{CIELAB2000} > 3$) only for untreated thermally weathered mock-ups. It is worth noting that the colour change determined for all treated samples was negligible ($\Delta E_{CIELAB2000} < 2.5$, Table S4 in the SI).

Materials and methods

Reagents and solvents were purchased from Carlo Erba, Fluorochem, TCL and used without further purification. The white marble variety "Statuario Michelangelo" from the Apuan Alps was obtained from Cava Franchi (Carrara, Italy). Prism-shaped specimens of different sizes (4.5 × 4.5 × 2.0 cm, 2.0 × 2.0 × 8.0 cm, and 2.0 × 2.0 × 2.0 cm) were sliced. Small irregular fragments (~1 cm^3 and weight ~3 g) were additionally used for the immersion treatment to perform the He pycnometry and Hg porosity determination. Carrara marble samples were partly naturally degraded; hence, only a mild thermal weathering was applied using a Carbolite CWF 1200 muffle furnace, where the temperature was ramped to 300 °C (2 h), held for 7 h, and cooled down to 25 °C in 2 h (Fig. S11).

Synthesis of ammonium hydrogen phenylphosphonate (1)

A phenylphosphonic acid aqueous solution (20.0 g, 0.127 mol, in 80 mL of distilled water) was slowly added to an ammonium carbonate solution (12.32 g, 0.127 mol, in 160 mL of the same solvent). The resulting solution was stirred for 3 h and then rotary evaporated to dryness to give a white solid. Yield: 21.33 g, 0.121 mol, (96.3%). M.p. = 260 °C. ^{1}H-NMR (DMSO-d_6): δ = 7.62 (m, 2H, Ar), 7.28 (m, 3H, Ar) ppm. ^{31}P-NMR (DMSO-d_6): δ = 8.40 (s, 1P, phosphonate) ppm. CP-MAS ^{13}C{^{1}H}-NMR: δ = 127.46 (s, Ar), 130.60 (s, Ar), 136.59 (d, Ar) ppm. CP-MAS ^{31}P{^{1}H}-NMR δ = 10.97 ppm. Elemental analysis (calcd for $C_6H_{10}PO_3N$): C 41.43 (41.15), H 5.18 (5.76), N 8.04 (8.00)%. FT-IR (KBr Pellet): $\tilde{\nu}$ = 3238 (m), 3047 (vw), 2783 (w), 2347 (w), 1970 (vw), 1911 (m), 1711 (m), 1439 (s), 1244 (s), 1144 (vs), 1036 (s), 920 (s), 748 (m), 700 (s), 571 (s), 526 (s), 498 (s), 440 (w) cm^{-1}.

Synthesis of calcium phenylphosphonate dihydrate (2)

A weighed amount of compound **1** (5.00 g, 0.028 mol) was dissolved in 300 mL of distilled water under stirring. A stoichiometric amount (1.4 g, 0.014 mol) of calcium carbonate was added, and the suspension was stirred for 24 h. The resulting grainy white solid was separated by filtration and air dried. Yield: 2.90 g, 0.0148 mol, (89.3%). CP-MAS ^{13}C{^{1}H}-NMR δ = 129.00 (s, Ar), 131.68 (s, Ar), 139.12 (d, Ar) ppm. CP-MAS ^{31}P{^{1}H}-NMR δ = 13.27 ppm. Elemental analysis (calcd for $C_6H_9O_5PCa$): C 30.63 (31.04), H 3.32 (3.91)%. FT-IR (KBr Pellets): $\tilde{\nu}$ = 3576 (m), 3410 (m), 3190 (m), 3074 (m), 3055 (m), 1962 (vw), 1899 (vw), 1633 (w), 1484 (vw), 1437 (m), 1387 (vw), 1383 (vw), 1309 (vw), 1142 (s), 1122 (s), 1095 (s), 1082 (s), 1068 (s), 1030 (s), 993 (s), 926 (w), 841 (w), 748 (m), 723 (s), 698 (s), 598 (s), 555 (m), 538 (s), 468 (w) cm^{-1}.

Application of compound 1 *via* immersion treatment

The mock-up mass was stabilized in a thermostatic heater at 60 ± 2 °C. The specimens were then immersed in a 5.0% w/w solution of compound **1** (0.30 mol L^{-1}) and left in a static bath for 24 h, following a previously applied technique.[31–35] At the end of the treatment, the pH of the solution was measured (5.92) and the unreacted salts were washed with distilled water, and the pH and conductivity of the washing solutions were

monitored. Once the washing was completed, the specimens were air dried and subsequently kept in a thermostatic heather (60 °C) for 24 h.

Application of compound 1 *via* brushing treatment

The mock-up mass was stabilized in a thermostatic heather at 60 ± 2 °C. A 5.0% w/w solution of compound **1** (0.30 mol L^{-1}) was then applied using a brush with synthetic (polypropylene) bristles appropriately sized for the dimensions of the treated specimen. Each surface was treated with 10 brushstrokes, rotating the specimen by 90° between each stroke and giving a one-minute pause between each application, to allow the solution to be absorbed. Before repeating this process for the next surface, the mock-up was left under ambient conditions, until the treated surface appeared dry. At the end of the treatment, the specimens were wrapped with a layer of parafilm and left to rest for 24 h. Any unreacted salts were subsequently washed off with distilled water, while the pH and conductivity of the washing solutions were monitored. The specimens were air-dried and then placed in a thermostatic heather at 60 °C for 24 h.

Application of compound 1 *via* spraying treatment

The mock-up mass was stabilized in a thermostatic heater at 60 ± 2 °C. A 5.0% w/w solution of compound **1** (0.30 mol L^{-1}) was then applied until surface rejection using a pressure nebulizer, at a controlled distance of 20 cm and a total flow rate of 16.4(8) mL min^{-1}. This process was repeated 6 times for each surface of the test specimen, rotating it by 180° between each spray and giving a 5 minute interval between applications, to allow the solution to be absorbed. Before proceeding to treat the next surface, the mock-up was left under ambient conditions, until it appeared dry. At the end of the treatment, the specimens were wrapped with a layer of parafilm and left for 24 h. On the following day, any unreacted salts were washed off with distilled water, and the pH and conductivity of the washing solutions were noted. The specimens were then left to air dry, before being placed into a thermostatic heather at (60 °C) for 24 h.

Physico-chemical characterization

Elemental analyses were carried out with a 2400 series II CHNS/O elemental analyser (T = 925 °C). Melting points were recorded using a FALC melting point apparatus, mod. C (25–300 °C). FT-IR spectra (KBr beam-splitter, KBr windows, 4000–400 cm^{-1}, resolution 4 cm^{-1}) were recorded using a Thermo-Nicolet 5700 spectrometer at room temperature on KBr pellets of the analysed samples. Electronic absorption spectra were recorded at 25 °C in a quartz cell (10.00 mm optical path) using a Thermo Evolution 300 (190–600 nm) spectrophotometer. ^{1}H-NMR, ^{13}C-NMR, ^{31}P-NMR measurements were carried out in DMSO-d_6 at 25 °C, using a Bruker Avance III HD 600 MHz (14.1 T) spectrometer at an operating frequency of 600.15 MHz. Chemical shifts are reported in ppm (δ) and are calibrated to the solvent residue. Solid-state NMR spectra were acquired with the same instrument (Bruker Avance III HD 600 MHz spectrometer) operating at frequencies of 242.94 MHz for ^{31}P-NMR and 150.15 MHz for ^{13}C-NMR. The instrument was equipped with a 2.5 mm CP-MAS H/X VTN solid-state sample probe. The magic angle (54.74°) was calibrated on the ^{79}Br signal of a standard KBr sample, while field calibration and probe shimming were performed using a standard adamantane sample. The samples, in the form of finely ground powder, were packed in zirconia rotors with an inner diameter of 2.5 mm and an inner volume of approximately 14 μL. Spectra were acquired with rotation frequency at a magic angle of 15 kHz. The cross-polarization (CP) technique was used for the measurements, in which conditions were determined for the two nuclei, using an adamantane standard (^{13}C) and an ammonium dihydrogen phosphate (^{31}P) standard. Solubility and K_{sp} values were evaluated spectrophotometrically at 25 °C on filtered saturated aqueous solutions, after recording a calibration curve. The pH of the solutions was determined using a Hanna 112 pH-meter. Conductivity measurements were carried out with a Crison GLP instrument, after calibration with standard solution of KCl.

3D Electron diffraction (3D-ED)

3D ED measurements were conducted using a Rigaku Synergy-ED electron diffractometer (LaB_6 200 kV), equipped with a Rigaku HyPix hybrid pixel area array detector. Grid (lacey carbon coated copper TEM grids; Agar Scientific, UK) loading was achieved by first gently grinding compound **2** between glass slides and then lightly dabbing the grid into these solids. The loaded grid was then mounted within a Gatan Elsa cryogenic holder (model 698) and introduced into the instrument *via* cryo-transfer at 175(5) K. Prior to exposing the grid to the column, the holder was held within the airlock (for approx. 15 min) to sublime any ice crystals which may have formed on the grid during transfer. Data collections were performed in continuous rotation mode with selected area aperture (diameter of approximately 2 μm in the image plane) using CrysAlisPRO (v1.171.44.66a)[77] at 175(5) K.

Several particles were surveyed and one data collection was chosen for structure determination and refinement. The dataset was indexed, reduced, integrated, and scaled using CrysAlisPRO (v1.171.44.90a)[77] and SCALE3 ABSPACK implemented therein. Where necessary, frames were rejected during the processing stage due to holder shadowing and similar effects. The structure was solved using ShelXT[78] and refined kinematically using ShelXL[79] within the Olex2 GUI (v1.5)[80,81] using published scattering factors for electrons.[82]

Refinements were performed in the presence of an extinction correction parameter to broadly account for dynamical effects. Hydrogen atoms were placed and refined geometrically constrained, their distances fixed to published X–H bond lengths for neutron diffraction,[83] and their ADPs refined isotropically using a riding model.

Crystal data: $C_6H_9CaO_5P$, M_r = 232.18, orthorhombic, *Pbca* (no. 61), a = 29.55 Å, b = 10.95 Å, c = 5.65 Å, $\alpha = \beta = \gamma = 90°$, V = 1829.4 Å^3, T = 175(2) K, Z = 8, Z' = 1.Table S2 reports experimental parameters from the used dataset. Complete

experimental and refinement information is contained in the deposited CIFs along with structure factors and embedded .RES files.

Powder X-ray diffraction (PXRD)

PXRD analyses were carried out at room temperature using a Bruker D8 Advance diffractometer equipped with a CuKα radiation source, operating at 40 kV and 40 mA, and a LynxEyE XE-T position-sensitive detector (PSD). Marble stone mock-ups were examined by placing the bulk samples onto a UMC *xyz* motorized stage, allowing for direct measurements on the stone surface. Proper alignment with the diffractometer geometry was ensured before data collection, which was carried out over a 2θ range of 3–60° with a fixed sample illumination length of 18 mm by means of motorized slits. For compounds **1** and **2**, PXRD data were collected using a conventional PTFE specimen holder over a 2θ range of 3–50°, with a step size of 0.03° and a counting time of 2 s per step. Rietveld refinement of the experimental diffraction pattern for **2** was performed using TOPAS v6,[84,85] based on the structural model obtained from 3D ED analysis.[86] In particular, Rietveld refinement was carried out with absorption correction and preferred orientation modelling, which notably affected the (200) reflection at ∼6°. The final values were: R_{wp} = 5.65%, R_{exp} = 1.56%, and GOF = 3.62. Visual inspection of the fit confirms that the model adequately reproduces the experimental pattern, with no significant unindexed peaks or evidence of secondary phases. The elevated value of the Goodness of Fit (GOF) is likely due to residual effects of preferred orientation.

Optical microscopy (OM) and scanning electron microscopy (SEM)

Examinations of the surfaces were carried out by OM using a Zeiss Axioskop 40 optical microscope equipped with a Zeiss camera AxioCam HR, while SEM investigations were performed with a Zeiss Evo LS15 microscope equipped with a LaB_6 filament as the electron source (operating at 20.00 kV) and a solid-state detector with a window of 50 mm^2. Prior to examination, the samples were homogenously gold coated using a Leica EM SCD005 sputter coater, operating for 80 s, with a current of 50 mA, a working distance of 50 mm, and a pressure of 0.05 mbar.

Ultrasonic measurements

Ultrasonic pulse velocity (v_{uts}) measurements were carried out before and after each treatment using a CNS Electronics Pundit tester (accuracy ± 0.1 ms). 150 MHz (**1**), 11.82 mm ∅ transducers were attached to the stone surface with Henkel Sichozell Kleister (carboxymethyl cellulose) paste to enhance the transducer-stone coupling. Three measurements were made directly and consecutively along the horizontal axis and then averaged. The results were used to calculate the Young's elastic modulus (E_d) with the following equation:

$$E_d = \rho \cdot V_p^2 \frac{(1+\delta)(1-2\delta)}{(1-\delta)}$$

where ρ is the sample skeletal density, determined by He pycnometry, and δ is the Poisson coefficient (δ_{marble} = 0.29).[87]

Colorimetric measurements

Colorimetric measurements were carried out using a Konica Minolta CM-700d spectrophotometer (illuminant D65), setup to carry out 6 measurements on each point. The results were evaluated as L^* (brightness), a^* (redness colour), and b^* (yellowness colour) coordinates. The total colour difference ΔE was calculated according to the CIELAB76 and CIELAB2000 colour space standards.[88]

Hygric measurements

Skeletal density ($\rho_{skeletal}$), bulk density (ρ_{bulk}), compactness index (I_c) and water open porosity index ($\Phi\%_{H_2O}$) were determined with a water saturation experiment. Before the test, the specimens were brought to constant mass in an oven at T = 60 ± 2 °C. Weighed samples were immersed in distilled H_2O for 24 h. The specimens were subsequently weighed on a hydrostatic balance and an analytical balance after having gently buffered the surfaces with a humid cloth. Based on the three masses measured, it was possible to calculate the following parameters:

$$\rho_{skeletal} = \frac{m_i}{m_{idr} - (m_{ps} - m_i)} \times \rho_{H_2O}$$

$$\rho_{bulk} = \frac{m_i}{m_{hydr}} \times \rho_{H_2O}$$

$$I_c = \frac{\rho_{skeletal}}{\rho_{bulk}} \times 100 \quad \Phi\% = \frac{(m_{ps} - m_i)}{(m_{ps} - m_{hydr})} \times 100$$

where m_i is the initial mass of the dry specimen, m_{ps} is the specimen mass after saturation with water, and m_{hydr} is the specimen mass weighed on the hydrostatic balance.

The skeletal density ($\rho_{skeletal}$), used for the calculation of the Young's elastic modulus, was determined using a Micromeritics AccuPyc II 1340 helium pycnometer, equipped with a 3.5 cm^3 sample holder cell. The measurements were carried out on stone fragments of 1 $cm^3 < V < 2$ cm^3. For each treatment, three fragments were selected, and five density measurements were performed on each.

Capillary water uptake tests were performed in accordance with the European Standard UNI EN 15801:2010.[89] The samples were dried at 60 °C for 24 h. The water absorption curve is expressed as Q (kg m^{-2}) for the *y*-axis *vs.* the square root of the absorption time ($t^{1/2}$) for the *x*-axis. The curves shown in Fig. S18 in the SI have absorption time reported in the *x*-axis expressed simply in hours (t) to better understand the span necessary for the desorption. The slope of the curve in the initial steep region is the capillary absorption coefficient CA, calculated using the following equation:

$$CA = \frac{Q_1 - Q_0}{t_1^{\frac{1}{2}} - t_0^{\frac{1}{2}}}$$

Drying experiments were carried out according to NorMaL 29/88.[90]

Soaked samples were weighed at increasing time intervals. The drying index (DI) was calculated by using the following equation:

$$\mathrm{DI} = \frac{\int_{t_i}^{t_f} f(\mathrm{wt})\mathrm{d}t}{\mathrm{wt}_{\max} \times t_f}$$

on a time interval ranging between t_i and t_f; $\mathrm{wt}_{\max}$ is the maximum water content at the initial testing time.[90] Vacuum water absorption tests were performed on all samples according to UNE EN 1936:2010 (pressure = 0.2 kPa).[91] From this free-water saturation method through Archimedes' principle and buoyancy techniques, the open porosity of the stone samples can also be determined by:[92]

$$\Phi\%_{\mathrm{H_2O\ vac}} = \frac{m_s - m_d}{m_s - m_h} \times 100$$

where m_d, m_h, and m_s are the mass values of the dry and saturated specimen in water and air, respectively. From these measurements, the skeletal (ρ_{skeletal}) and bulk density (ρ_{bulk}) were determined.[93] Measurements of liquid water permeability were carried out with the Karsten test, according to the UNI EN 16302:2013 standard.[94] Measurements were repeated on 3 specimens measuring 4.5 × 4.5 × 2.0 cm for each lithotype under study. Karsten tubes (8 mL of capacity, 3 cm base diameter) were placed on top of the specimens, with a perfect adhesion of the base ensured by a clay plastiform polymer. The tube was filled with distilled water, allowing the water to flow through the material. To ensure constant water head pressure, the water volume was restored after every 0.5 mL permeated. The volumes of water dispensed were recorded at time intervals of 2, 4, 6, 10, 15, and 30 min. The collected data were used to determine the liquid water permeability index (μ, kg m^{-2} h$^{-1/2}$) and the water flow speed (mL min^{-1}).

Vapour permeability tests were performed according to the UNI EN 15803:2010 standard.[95] Each mock-up (4.5 × 4.5 × 2.0 cm) was inserted inside a sample holder, with an internal chamber half-filled with distilled water. All the measuring systems were kept under stable conditions of humidity (60 ± 5%) and temperature (21 ± 2 °C), and the weight of the system was measured every 24 h over a week. The permeability coefficient (δ_p) was then determined with the following equations:

$$W_p = \frac{G}{A\Delta p_v} \quad \delta_p = W_p \times D$$

where G is the vapour flown through the sample (kg s^{-1}); W_p is the water penetration (kg m^{-2} s^{-1} Pa^{-1}); Δp_v is the pressure difference between the two sides of the material (Pa); A is the test area in m^2; and D is the average width of the sample (m). The G value can be graphically determined by plotting the system mass variation against the square root of time. By simply dividing the value of δ_p by the air vapour water permeability coefficient (1.93 × 10^{-10} kg m^{-2} s^{-1} Pa^{-1}), the vapour water resistance factor μ was calculated.

Mercury intrusion porosimetry (MIP)

MIP measurements were carried out on small fragments (<1 cm^3) of stone using a Micromeritics Autopore IV 9520 with a maximum pressure of 414 MPa. This technique is based on the Washburn equation:[96]

$$P = 2\gamma \cdot \cos\frac{\theta}{r_c}$$

where γ is the superficial tension of Hg, θ is the contact angle of Hg, and r_c is the radius of the cylinder tube where the sample is inserted during the measurement. This measurement allowed the evaluation of the total open porosity, pore size discriminations of the pore, and cumulative total volume of the samples.

Thermogravimetric analysis

TGA measurements were performed using a PerkinElmer STA 6000 Simultaneous Thermal Analyser. For all analyses, 5 mg of the sample were weighed on an alumina crucible and the simultaneous TGA-DSC thermograms from 25 to 850 °C with a gradient of 10 °C per min using a 40 mL min^{-1} N_2 flow were recorded.

Mechanical measurements

Pull-off tests were performed according to standard UNI EN 1015-12:2000 and used to evaluate the resistance to tearing of the sample.[97] Steel stubs, 20 mm in diameter, were grit blasted and attached to samples (3 prisms of 8.0 × 8.0 × 2.0 cm) with an epoxy adhesive to form a butt joint. After the curing of the adhesive, the joints were then pulled into a universal testing machine fitted with a 5 kN load cell and tested at a rate of 2 mm min^{-1} at 25 °C. The tensile strength index (f_h, N mm^{-2}) was then determined using the strength necessary to obtain the pull-off of the attached steel tubes.

Shore hardness C and D measurements were performed on mock-up surfaces upon treatment (minimal sampling of three measurements per surface) with Shore durometers (LC display meter 0–100 HD and 0–100 C), equipped with a standardised indenting foot of a hardened steel rod as required by ASTM D2240.[98] Shore scale D: sharp 30° cone, and a 0.1 mm radius tip, a force of 44.5 N in a scale ranging between 0 and 100 HD. Shore scale C flat 35° cone, and a 0.79 mm radius tip, a force of 44.5 N in a scale ranging between 0 and 100 HC.

Surface properties

Superficial tension measurements were made following standard UNI EN 828:2013 using a Nikon D800 camera equipped with 105 mm macro lens and using white LED lights as the illuminating source.[99] A drop of 0.6 μL was released on a regular surface from ~1 mm distance and pictures were recorded after 2, 30 and 60 s. Using the software BMS.pix3, the collected pictures were then elaborated determining the contact angle for both sides of any drop. For each kind of treated material, the test was applied on a regular surface of three different samples and the results averaged. The surface roughness of the specimens was investigated by means of a

Mitutoyo SJ-201 portable surface roughness tester according to the JIS 01 ISO standard. Two faces for each specimen were analysed ten times, with a 1 mm shift after each measurement.

Accelerated aging

All the aging treatments were performed on sets of three $8 \times 2 \times 2$ cm mock-ups. Thermal shocks were performed following the international EN 14066:2014 standard.[73] The specimens were dried in a ventilated oven at 40 ± 5 °C for one week and then cooled to ambient temperature before starting the cycles. The dried specimens were subjected to changes of temperature according to the following procedure: 18 ± 1 h inside a ventilated oven at 70 ± 5 °C; immediately followed by 6 ± 0.5 h completely submerged in distilled water (20 ± 5 °C). Both in the oven and in the water container, the specimens were placed 50 mm from one another and from the wall. In the water container, specimens were placed on a support located at the bottom, filled with distilled water at a height of 60 ± 10 mm over the height of the submerged specimens. After the 21st cycle, the specimens were dried to constant mass at 70 ± 5 °C.

Frost resistance of the mock-ups were determined following the international standard EN 12371:2010.[74] The specimens were dried in a ventilated oven at 70 ± 5 °C to constant mass. The specimens were placed in a container along the vertical axis without coming in contact with another (50 mm) and with the walls (20 mm). One cycle consists of a 6 h freezing period in air, followed by a 6 h thawing with the specimen immersed in water. After each cycle, the mock-ups were rotated by 180° and placed in the same position. After the 21st cycle, the specimens were dried to constant mass at 70 ± 5 °C.

Acid attacks were performed following the procedure published by Pasapergio *et al.*:[75] before each test, an Hanna 112 pH–meter was calibrated at pH 4, 7, and 10 buffer solutions. Nitric acid (HNO_3) was used to adjust the solution pH to 5. The HNO_3 solution was continuously stirred to allow equilibration before the tests. Untreated and treated small specimens were immersed in separate beakers submerged in such solution of HNO_3 at an initial pH 5 and kept in rotatory motion for 24 h with a magnetic stirrer. Subsequently, the samples were rinsed with distilled water, dried at room temperature until constant weight and observed by SEM as described above. The mock-ups were also characterised by means of superficial hardness determinations, rugosimetry, colourimetry, and ultrasonic speed propagation measurement.

Conclusions

In this paper, we report the synthesis, characterization, and stone treatment tests of the novel salt ammonium hydrogen phenylphosphonate (NH_4)($HPhPO_3$) (**1**) as a conservation agent for Statuario white Carrara marble. Compound **1** reacts readily with calcium carbonate and calcite to form calcium phenylphosphonate dihydrate $Ca(PhPO_3)\cdot 2H_2O$ (**2**). The crystal structure of compound **2** was elucidated by means of 3D electron diffraction (3D ED). Although this technique has been utilized in the field of cultural heritage in recent years, to the best of our knowledge, this is the first reported application of 3D ED as a structural characterization technique in this context. PXRD measurements showed that the treatment of Carrara marble with compound **1** resulted in the formation of a microcrystalline coating of compound **2**, and no other species were identified on the surface.

Coating properties strongly depend on the application technique. Brushing and spraying application methods proved more effective in restoring the properties of weathered marble, with treated samples exhibiting dynamic, structural, and hygric properties close to those of the pristine samples. Spraying also increased the surface hydrophobicity, as evidenced by the measured contact angle values. The deposited patinas, regardless of the treatment method, demonstrated the ability to form a homogeneous phase, with crystals aggregated into a compact layer. This property ensures that subsequent applications of the same treatment can still achieve consolidation, even over a pre-existing coating. These results suggest that both brushing and spraying methods produce a more homogeneous coating than immersion, allowing in some cases for precise treatment design to achieve surface hydrophobization. The consolidation effect was accompanied by no significant changes in colour or vapour permeability, demonstrating the high compatibility of the treatment with the carbonate substrates. The results of this research prove ammonium hydrogen phenylphosphonate as an innovative, economically affordable, and soluble consolidant for the conservation of carbonate stone materials. It overcomes several limitations of currently established consolidants (such diammonium hydrogen phosphate, DAP), whose treatments on carbonate stones lead to the formation of hydroxyapatite (HAP) accompanied by non-stoichiometric products, such as $Ca_8(HPO_4)_2(PO_4)_4\cdot 5H_2O$ and $CaHPO_4\cdot 2H_2O$ (brushite), some of which are more soluble than calcite.

A comparison between ammonium hydrogen phenylphosphonate and diammonium hydrogen phosphate exemplifies the subtle role played by the anion size in tailoring the chemical–physical properties and reactivity of the resulting calcium salts.

Future studies may focus on long-term durability assessments and the potential for widespread application to other different lithotypes and ancient lime mortars used in historical monuments.

Author contributions

M. A., P. M., M. C. A., and D. G.: conceptualization; M. A., P. M., and D. G.: supervision; S. M., G. C., S. C., E. P., A. P., S. J. C., J. B. O., and D. N. R: methodology; all authors: investigation; S. M., M. A., G. E., and E. P.: data curation; M. A., S. M., E. P., and V. L.: writing; all authors: writing – review and editing.

Conflicts of interest

There are no conflicts to declare.

Data availability

The data supporting this article have been included as part of the supplementary information (SI). Supplementary information is available. See DOI: https://doi.org/10.1039/d5ma01116g.

CCDC 2473954 (**2**) contains the supplementary crystallographic data for this paper.[100]

3D ED raw data are available on Zenodo (https://doi.org/10.5281/zenodo.16742748).

Acknowledgements

We thank the Università degli Studi di Cagliari for financial support and CeSAR (Centro Servizi d'Ateneo per la Ricerca) of the University of Cagliari, Italy, for NMR and PXRD measurements. CINECA is kindly acknowledged for the computational resources on the GALILEO100 supercomputer accessed within the ISCRA Class C project "A DFT approach to the conservation of cultural heritage: interaction of new consolidating and protecting agents with carbonate stones and mortars" (LithoDFT). PhD grant statement for S. M.: this article was produced while attending the PhD programme in Chemical Sciences and Technology at the University of Cagliari, Cycle XXXVIII, with the support of a scholarship financed by the Ministerial Decree no. 351 of 9th April 2022, based on the NRRP-funded by the European Union-NextGeneration-EU-Mission 4 "Education and Research", Investment 4.1"Extension of the number of research doctorates and innovative doctorates for public administration and cultural heritage. Fondazione di Sardegna (FdS Progetti Biennali di Ateneo, annualità 2022, grant no. F73C23001580007) is kindly acknowledged for financial support. D. N. R., J. B. O., and S. J. C. acknowledged the EPSRC for continued funding for the UK National Crystallography Service (NCS) and the National Electron Diffraction Facility (NEDF). D. N. R. is grateful to the 3D ED community for ongoing and robust input to the developing field of electron diffraction, especially Dr Jere Tidey, Dr Arianna Lanza, and Dr Claire Wilson.

References

1 A. Gabrielli, G. Ugolotti, G. Masi and E. Sassoni, Resistance of consolidated lime mortars to freeze–thaw and salt crystallization cycles by different accelerated durability tests, *Mater. Struct.*, 2024, **57**, 70.
2 B. Doherty, M. Pamplona, R. Selvaggi, C. Miliani, M. Matteini, A. Sgamellotti and B. Brunetti, Efficiency and resistance of the artificial oxalate protection treatment on marble against chemical weathering, *Appl. Surf. Sci.*, 2007, **253**, 4477–4484.
3 İ. Uğur and H. Ö. Toklu, Effect of Multi-Cycle Freeze-Thaw Tests on the Physico-Mechanical and Thermal Properties of Some Highly Porous Natural Stones, *Bull. Eng. Geol. Environ.*, 2019, **79**, 255–267.
4 S. Columbu, M. Usai, C. Rispoli and D. Fancello, Lime and Cement Plasters from 20th Century Buildings: Raw Materials and Relations between Mineralogical–Petrographic Characteristics and Chemical–Physical Compatibility with the Limestone Substrate, *Minerals*, 2022, **12**(2), 226.
5 S. Columbu, P. Meloni, G. Carcangiu and D. Fancello, Workability and chemical-physical degradation of limestone frequently used in historical Mediterranean architecture, Imeko TC 4 International Conference on Metrology for Archaeology and Cultural Heritage, 2020, pp. 189–195.
6 S. Columbu, S. Carboni, S. Pagnotta, V. Palleschi and A. Usai, Laser-Induced Breakdown Spectroscopy analysis of the limestone Nuragic statues from Mont'e Prama site (Sardinia, Italy), *Spectrochim. Acta, Part B*, 2018, **149**, 62–70.
7 S. Naidu, J. Blair and G. W. Scherer, Acid-Resistant Coatings on Marble, *J. Am. Ceram.*, 2016, **99**, 3421–3428.
8 N. Plummer and E. Busenberg, The Solubilities of Calcite, Aragonite and Vaterite in CO_2–H_2O Solutions between 0 and 90 °C, and an Evaluation of the Aqueous Model for the System $CaCO_3$–CO_2–H_2O, *Geochim. Cosmochim. Acta*, 1982, **46**, 1011–1040.
9 M. F. Salinas-Nolasco, J. Méndez-Vivar, V. H. Lara and P. Bosch, Passivation of the calcite surface with malonate ion, *J. Colloid Interface Sci.*, 2004, **274**, 16–24.
10 M. F. Salinas-Nolasco, J. Méndez-Vivar, V. H. Lara and P. Bosch, Passivation of the calcite surface with phenylmalonate and benzylmalonate ions, *J. Colloid Interface Sci.*, 2005, **286**, 68–81.
11 E. D. Witte, Soluble Nylon as Consolidation Agent for Stone, *Stud. Conserv.*, 1975, **20**, 30–34.
12 C. Conti, I. Aliatis, M. Casati, C. Colombo, M. Matteini, R. Negrotti, M. Realini and G. Zerbi, Diethyl oxalate as new potential conservation product for decayed carbonatic substrates, *J. Cult. Herit.*, 2014, **15**, 336–338.
13 A. Dal Pozzo, G. Masi, E. Sassoni and A. Tugnoli, Life cycle assessment of stone consolidants for conservation of cultural heritage, *Build. Environ.*, 2024, **249**, 111153.
14 M. Matteini, Inorganic treatments for the consolidation and Protection of stone artefacts and mural paintings, *Conserv. Sci. Cult. Herit.*, 2008, **8**, 13–27.
15 D. G. Kanellopoulou and P. G. Koutsoukos, Inorganic Coatings for the Protection of Marble Surfaces from Deterioration, *Rev. Conserv.*, 2005, **11**, 161–168.
16 E. Hansen, E. Doehne, J. Fidler, J. Larson, B. Martin, M. Matteini, C. Rodriguez-Navarro, E. S. Pardo, C. Price, A. de Tagle, J. M. Teutonico and N. Weiss, A Review of Selected Inorganic Consolidant and Protective Treatments for Porous Calcareous Materials, *Rev. Conserv.*, 2003, **4**, 13–25.
17 S. Columbu, C. Lisci, F. Sitzia and G. Buccellato, Physical–mechanical consolidation and protection of Miocenic limestone used on Mediterranean historical monuments: the case study of Pietra Cantone (Southern Sardinia, Italy), *Environ. Earth Sci.*, 2017, **76**(4), 148.
18 M. I. Daskalakis, A. Magoulas, G. Kotoulas, I. Catsikis, A. Bakolas, A. P. Karageorgis, A. Mavridou, D. Doulia and

F. Rigas, Pseudomonas, Pantoea and Cupriavidus isolates induce calcium carbonate precipitation for biorestoration of ornamental stone, *J. Appl. Microbiol.*, 2013, **115**, 409–423.

19 V. Daniele, G. Taglieri and R. Quaresima, The nanolimes in Cultural Heritage conservation: characterisation and analysis of the carbonatation process, *J. Cult. Herit.*, 2008, **9**, 294–301.

20 M. Licchelli, M. Malagodi, M. Weththimuni and C. Zanchi, Nanoparticles for conservation of bio-calcarenite stone, *Appl. Phys. A: Mater. Sci. Process.*, 2014, **114**, 673–683.

21 C. Rodriguez-Navarro, A. Suzuki and E. Ruiz-Agudo, Alcohol Dispersions of Calcium Hydroxide Nanoparticles for Stone Conservation, *Langmuir*, 2013, **29**, 11457–11470.

22 I. Natali, M. L. Saladino, F. Andriulo, D. Chillura Martino, E. Caponetti, E. Carretti and L. Dei, Consolidation and protection: recent advances for the conservation of the graffiti, Carceri dello Steri Palermo and of the 18th century lunettes, SS Giuda e Simone Cloister, Corniola (Empoli), *J. Cult. Herit.*, 2014, **15**, 151–158.

23 F. Jroundi, M. Schiro, E. Ruiz-Agado, K. Elert, I. Martín-Sánchez, M. T. Gonzales-Munoz and C. Rodriguez-Navarro, Protection and consolidation of stone heritage by self-inoculation of carbonatogenic bacterial communities, *Nat. Commun.*, 2017, **8**, 279.

24 P. Tiano, L. Biagiotti and G. Mastromei, Bacterial biomediated calcite precipitation for monumental stones conservation: methods of evaluation, *J. Microbiol. Methods*, 1999, **36**, 139–145.

25 N. Dhami, M. S. Reddy and A. Mukherjee, Biomineralization of calcium carbonates and their engineered applications: a review, *Front. Microbiol.*, 2013, **4**, 314.

26 D. Mudronja, F. Vanmeert, S. Fazinic, K. Janssens, D. Tibljias and V. Desnica, Protection of Stone Monuments Using a Brushing Treatment with Ammonium Oxalate, *Coatings*, 2021, **11**, 379.

27 W. H. McComas and W. Rieman, The Solubility of Calcium Oxalate Monohydrate in Pure Water and Various Neutral Salt Solutions at 25°, *J. Am. Chem. Soc.*, 1942, **64**, 2946–2947.

28 L. Brečević, D. Škrtić and J. Garside, Transformation of calcium oxalate hydrates, *J. Cryst. Growth*, 1986, **74**, 399–408.

29 D. Mudronja, F. Vanmeert, K. Hellemans, S. Fazinic, K. Janssens, D. Tibljas, M. Rogosic and S. Jakovljevic, Efficiency of applying ammonium oxalate for protection of monumental limestone by poultice, immersion and brushing methods, *Appl. Phys. A: Mater. Sci. Process.*, 2013, **111**, 109–119.

30 A. E. Hill and E. F. Distler, The solubility of ammonium oxalate in water, *J. Am. Chem. Soc.*, 1935, **57**, 2203–2204.

31 L. Maiore, M. C. Aragoni, G. Carcangiu, O. Cocco, F. Isaia, V. Lippolis, P. Meloni, A. Murru, E. Tuveri and M. Arca, Synthesis, characterisation and DFT-modelling of novel agents for the protection and restoration of historical calcareous stone substrates, *J. Colloid Interface Sci.*, 2015, **448**, 320–330.

32 L. Maiore, M. C. Aragoni, G. Carcangiu, O. Cocco, F. Isaia, V. Lippolis, P. Meloni, A. Murru, A. M. A. Slawin, E. Tuveri, J. D. Woollins and M. Arca, Oxamate salts as novel agents for the restoration of marble and limestone substrates: case study of ammonium *N*-phenyloxamate, *New J. Chem.*, 2016, **40**, 2768–2774.

33 A. Pintus, M. C. Aragoni, G. Carcangiu, L. Giacopetti, F. Isaia, V. Lippolis, L. Maiore, P. Meloni and M. Arca, Density functional theory modelling of protective agents for carbonate stones: a case study of oxalate and oxamate inorganic salts, *New J. Chem.*, 2018, **42**, 11593–11600.

34 M. C. Aragoni, L. Giacopetti, M. Arca, G. Carcangiu, S. Columbu, D. Gimeno, F. Isaia, V. Lippolis, P. Meloni, A. Navarro Ezquerra, E. Podda, J. Rius, O. Vallcorba and A. Pintus, Ammonium monoethyloxalate (AmEtOx): a new agent for the conservation of carbonate stone substrates, *New J. Chem.*, 2021, **45**, 5327–5339.

35 A. Pintus, M. C. Aragoni, G. Carcangiu, V. Caria, S. J. Coles, E. Dodd, L. Giacopetti, D. Gimeno, V. Lippolis, P. Meloni, S. Murgia, A. Navarro Ezquerra, E. Podda, C. Urru and M. Arca, Ammonium *N*-(pyridin-2-ylmethyl)oxamate (AmPicOxam): A Novel Precursor of Calcium Oxalate Coating for Carbonate Stone Substrates, *Molecules*, 2023, **28**, 5768.

36 E. Sassoni, S. Naidu and G. W. Scherer, The use of hydroxyapatite as a new inorganic consolidant for damaged carbonate stones, *J. Cult. Herit.*, 2011, **12**, 346–355.

37 M. Desouky, M. S. Aljawad, A. Abduljamiu, T. Solling, D. Al-Shehri, M. J. AlTammar and K. M. Alruwaili, Temperature, pressure, and duration impacts on the optimal stiffening of carbonates aged in diammonium phosphate solution, *Sci. Rep.*, 2024, **14**, 6444.

38 M. Balonis, M. Ma and I. Kakoulli, Phase relations in the calcium carbonate/ammonium phosphate system under aqueous conditions and 25 °C, *J. Am. Ceram. Soc.*, 2020, **103**, 3837–3850.

39 E. Possenti, C. Colombo, C. Conti, L. Gigli, M. Merlini, J. Rikkert Plaisier, M. Realini, D. Sali and G. D. Gatta, Diammonium hydrogenphosphate for the consolidation of building materials. Investigation of newly-formed calcium phosphates, *Constr. Build. Mater.*, 2019, **195**, 557–563.

40 M. Matteini, S. Rescic, F. Fratini and G. Botticelli, Ammonium phosphates as consolidating agents for carbonatic stone materials used in architecture and cultural heritage: preliminary research, *Int. J. Archit. Herit. Conserv. Anal. Restor.*, 2011, **5**, 717–736.

41 E. Sassoni, Hydroxyapatite and Other Calcium Phosphates for the Conservation of Cultural Heritage: A Review, *Materials*, 2018, **11**, 557.

42 E. Sassoni, G. Ugolotti and M. Pagani, Nanolime, nanosilica or ammonium phosphate? Laboratory and field study on consolidation of a byzantine marble sarcophagus, *Constr. Build. Mater.*, 2020, **262**, 120784.

43 S. Mandel and A. C. Tas, Brushite ($CaHPO_4{\cdot}2H_2O$) to octacalcium phosphate ($Ca_8(HPO_4)_2(PO_4)_4{\cdot}5H_2O$) transformation in DMEM solutions at 36.5 °C, *Mater. Sci. Eng., C*, 2010, **30**, 245–254.

44 W. F. Jaynes, P. A. Moore, Jr. and D. M. Miller, Solubility and Ion Activity Products of Calcium Phosphate Minerals, *J. Environ. Quality*, 1999, **28**, 530–536.
45 J. R. Meyer-Fernandes and A. Vieyra, Pyrophosphate formation from acetyl phosphate and orthophosphate: evidence for heterogeneous catalysis, *Arch. Biochem. Biophys.*, 1988, **266**, 132–141.
46 A. Murru and R. Fort, Diammonium hydrogen phosphate (DAP) as a consolidant in carbonate stones: impact of application methods on effectiveness, *J. Cult. Herit.*, 2020, **42**, 45–55.
47 S. Naidu and G. W. Scherer, Nucleation, growth and evolution of calcium phosphate films on calcite, *J. Colloid Interface Sci.*, 2014, **435**, 128–137.
48 E. Possenti, C. Colombo, D. Bersani, M. Bertasa, A. Botteon, C. Conti, P. P. Lottici and M. Realini, New insight on the interaction of diammonium hydrogen phosphate conservation treatment with carbonatic substrates: a multi-analytical approach, *Microchem. J.*, 2016, **127**, 79–86.
49 G. Graziani, E. Sassoni, E. Franzoni and G. W. Scherer, Hydroxyapatite coatings for marble protection: optimization of calcite covering and acid resistance, *Appl. Surf. Sci.*, 2016, **368**, 241–257.
50 C. Pesce, L. M. Moretto, E. F. Orsega, G. L. Pesce, M. Corradi and J. Weber, Effectiveness and Compatibility of a Novel Sustainable Method for Stone Consolidation Based on Di-Ammonium Phosphate and Calcium-Based Nanomaterials, *Materials*, 2019, **12**, 3025.
51 E. Sassoni, G. Graziani, E. Franzoni and G. W. Scherer, Calcium phosphate coatings for marble conservation: influence of ethanol and isopropanol addition to the precipitation medium on the coating microstructure and performance, *Corros. Sci.*, 2018, **136**, 255–267.
52 B. Sena da Fonseca, A. P. Ferreira Pinto, A. Rodrigues, M. Mucha and M. F. Montemor, Ability of novel consolidants to improve cohesion of carbonate stones: dependence on pore-shape, aging conditions and treatment procedures, *J. Cult. Herit.*, 2022, **55**, 95–106.
53 B. Sena, da Fonseca, Current Trends in Stone Conservation Research: An Overview and Discussion, *Buildings*, 2023, **13**, 403.
54 N. Harsági and G. Keglevic, The Hydrolysis of Phosphinates and Phosphonates: A Review, *Molecules*, 2021, **26**, 2840.
55 A. P. Ferreira Pinto and J. Delgado Rodrigues, Stone consolidation: the role of treatment procedures, *J. Cult. Herit.*, 2008, **9**, 38–53.
56 Z. Lin, X.-Q. Lei, S.-D. Bai and S. W. Ng, Ammonium benzenephosphonate, *Acta Crystallogr.*, 2008, **E64**, o1607.
57 J. R. Weakley, Benzenephosphonic acid, *Acta Crystallogr.*, 1976, **B32**, 2889–2890.
58 M. Aragon, S. E. J. Bowman, C.-H. Chen, M. J. de la Cruz, D. A. Decato, E. T. Eng, K. M. Flatt, S. Gulati, Y. Li, C. J. Lomba, B. Mercado, J. Miller, L. Palatinus, W. J. Rice, D. Waterman and C. M. Zimanyi, Applying 3D ED/MicroED workflows toward the next frontiers, *Acta Crystallogr.*, 2024, **C80**, 179–189.
59 P. Pratim Das, A. Ponce-Pedraza, E. Mugnaioli and S. Nicolopoulos, Electron Diffraction and Structural Imaging II, *Symmetry*, 2022, **14**, 1287.
60 P. Chen, Y. Liu, C. Zhang, F. Huang, L. Liu and J. Sun, Crystalline Sponge Method by Three-Dimensional Electron Diffraction, *Front. Mol. Biosci.*, 2021, **8**, 821927.
61 S. Nicolopoulos, P. P. Das, A. G. Pérez, N. Zacharias, S. T. Cuapa, J. A. A. Alatorre, E. Mugnaioli, M. Gemmi and E. F. Rauch, Novel TEM Microscopy and Electron Diffraction Techniques to Characterize Cultural Heritage Materials: From Ancient Greek Artefacts to Maya Mural Paintings, *Scanning*, 2019, 4870695.
62 S. N. Black and L. Seton, Curating Morphological Data: From the Compendium of P. von Groth to the Cambridge Structural Database, *Cryst. Growth Des.*, 2024, **24**(12), 5051–5060.
63 W. Köhler, *Untersuchungen zu Verwitterungsvorgängen an Carrara-Marmor in Potsdam Sanssouci in Berichte zu Forschung und Praxis der Denkmalpflege in Deutschland*, Steinschäden—Steinkonservierung, 1991, pp. 50–54.
64 A. Ahmad, Investigation of marble deterioration and development of a classification system for condition assessment using non-destructive ultrasonic technique, *Mediterr. Archaeol. Archaeom.*, 2020, **20**, 75–89.
65 S. Siegesmund, K. Ullemeyer, T. Weiss and E. K. Tschegg, Physical weathering of marbles caused by anisotropic thermal expansion, *Int. J. Earth Sci.*, 2000, **89**, 170–182.
66 N. Ashurst and J. Kelly, in *The analytic approach to stone: its cleaning, repair and treatment, in Conservation of Building and Decorative Stone*, ed. F. J. Dimes and J. Ashurst, Routledge, 1998, vol. 2, pp. 240–243.
67 M. Laho, C. Franzen, R. Holzer and P. W. Mirwald, Pore and hygric properties of porous limestones: a case study from Bratislava, Slovakia, in *Natural Stone Resources for Historical Monuments*, ed. R. Prikryl and Á. Török, Geological Society of London, Special Publications, 2010, **333**, pp. 165–174.
68 E. Sassoni, G. Graziani and E. Franzoni, An innovative phosphate-based consolidant for limestone. Part 1: effectiveness and compatibility in comparison with ethyl silicate, *Constr. Build. Mater.*, 2016, **102**, 918–930.
69 G. Masi, A. Dal Pozzo, G. Ugolotti, A. Tugnoli and E. Sassoni, Choosing the consolidant for carbonate substrates: technical performance and environmental sustainability of selected inorganic and organic products, *Constr. Build. Mater.*, 2023, **407**, 133599.
70 Mineralogy Database, Available online: https://webmineral.com/(accessed on 20 February 2025).
71 W. S. Mokrzycki and M. Tatol, Color difference Delta E–A survey, *Mach. Graphics Vis.*, 2011, **20**, 383–411.
72 J. D. Rodrigues and A. Grossi, Indicators and ratings for the compatibility assessment of conservation actions, *J. Cult. Herit.*, 2007, **8**, 32–43.
73 EN 14066:2014, Natural stone test methods – Determination of resistance to ageing by thermal shocks, European Committee for Standardisation: Brussel, 2014.

74 EN 12371:2010, Natural stone test methods – Determination of frost resistance, European Committee for Standardisation: Brussel, 2010.
75 A. E. Papasergio, G. Ugolotti, M. Lessio and E. Sassoni, New insights on conservation of marble artworks from computational chemistry, *Mater. Today: Proc.*, 2023, DOI: 10.1016/j.matpr.2023.06.467.
76 S. Sugiyama, H. Nishioka, T. Moriga, H. Hayashi and J. B. Moffat, Ion–exchange properties of strontium hydroxyapatite under acidic conditions, *Separ. Sci. Technol.*, 1998, **33**, 1999–2007.
77 CrysAlisPRO, Rigaku Oxford Diffraction, 2024.
78 G. M. Sheldrick, SHELXT-Integrated Space-Group and Crystal Structure Determination, *Acta Crystallogr., Sect. A: Found. Adv.*, 2015, **71**, 3–8.
79 G. M. Sheldrick, Crystal structure refinement with ShelXL, *Acta Crystallogr., Sect. C: Struct. Chem.*, 2015, **71**, 3–8.
80 L. J. Bourhis, O. V. Dolomanov, R. J. Gildea, J. A. K. Howard and H. Puschmann, The anatomy of a comprehensive constrained, restrained refinement program for the modern computing environment-Olex2 dissected, *Acta Crystallogr., Sect. A: Found. Adv.*, 2015, **71**, 59–75.
81 O. V. Dolomanov, L. J. Bourhis, R. J. Gildea, J. A. Howard and H. Puschmann, OLEX2: a complete structure solution, refinement and analysis program, *J. Appl. Cryst.*, 2009, **42**, 339–341.
82 A. Saha, S. S. Nia and J. A. Rodríguez, Electron Diffraction of 3D Molecular Crystals, *Chem. Rev.*, 2022, **122**, 13883–13914.
83 F. H. Allen and I. J. Bruno, Bond lengths in organic and metal-organic compounds revisited: X–H bond lengths from neutron diffraction data, *Acta Crystallogr., Sect. B:Struct. Sci.*, 2010, **66**, 380–386.
84 R. E. Dinnebier, A. Leineweber and J. S. O. Evans, *Rietveld Refinement: Practical Powder Diffraction Pattern Analysis using TOPAS*, De Gruyter, Berlin, Boston, 2019.
85 A. A. Coelho, *TOPAS* and *TOPAS-Academic*: an optimization program integrating computer algebra and crystallographic objects written in C++, *J. Appl. Cryst.*, 2018, **51**, 210–218.
86 C. F. Macrae, I. Sovago, S. J. Cottrell, P. T. A. Galek, P. McCabe, E. Pidcock, M. Platings, G. P. Shields, J. S. Stevens, M. Towlera and P. A. Wood, Mercury 4.0: from visualization to analysis, design and prediction, *J. Appl. Cryst.*, 2020, **53**, 226–235.
87 M. Alber and U. Hauptfleisch, Generation and visualization of microfractures in Carrara marble for estimating fracture toughness, fracture shear and fracture normal stiffness, *Int. J. Rock Mech. Min. Sci.*, 1999, **36**, 1065–1071.
88 A. W. Hatheway and G. A. Kiersch. Engineering properties of rocks, in *Handbook of physical properties of rocks*, ed. R. S. Carmichael, CRC Press, Boca Raton FL, 1986, vol. 2, pp. 289–331.
89 EN 15801; Conservation of Cultural Property—Test Methods—Determination of Water Absorption by Capillarity. Ente Nazionale Italiano di Unificazione: Milan, Italy, 2010.
90 NORMAL 29/88; Misura Dell'indice di Asciugamento (Dryng Index). CNR-ICR (Consiglio Nazionale delle Ricerche—Istituto Centrale per il Restauro): Rome, Italy, 1988.
91 J. Grilo, P. Faria, R. Veiga, A. Santos Silva, V. Silva and A. Velosa, New Natural Hydraulic Lime mortars—Physical and microstructural properties in different curing conditions, *Constr. Build. Mater.*, 2014, **54**, 378–384.
92 EN 1936; Natural Stone Test Methods—Determination of Real Density and Apparent Density, and of Total and Open Porosity. Turkish Standard Institute: Ankara, Turkey, 2007.
93 C. Hall and A. Hamilton, Porosities of building limestones: using the solid density to assess data quality, *Mater. Struct. Constr.*, 2016, **49**, 3969–3979.
94 UNI EN 16302:2013, Conservation of cultural heritage – test methods – measurement of water absorption by pipe method, Ente Nazionale Italiano di Unificazione: Milan, Italy, 2013.
95 UNI EN 15803:2010, Conservation of cultural heritage – test methods – Determination of Water Vapor Permeability (dp), Ente Nazionale Italiano di Unificazione: Milan, Italy, 2010.
96 E. W. Washburn, The Dynamics of Capillary Flow, *Phys. Rev.*, 1921, **17**, 273–283.
97 EN 1015-12:2016, Methods of Test for Mortar for Masonry—Part 12: Determination of Adhesive Strength of Hardened Rendering and Plastering Mortars on Substrates. Ente Nazionale Italiano di Unificazione: Milan, Italy, 2016.
98 D2240-15, Standard Test Method for Rubber Property---Durometer Hardness, ASTM, West Conshohoken, United States, 2017.
99 UNI EN 828:2013, Adhesives – Wettability – Determination by measurement of the contact angle and free surface energy of the solid surface, Ente Nazionale Italiano di Unificazione: Milan, Italy, 2013.
100 CCDC 2473954: Experimental Crystal Structure Determination, 2026, DOI: 10.5517/ccdc.csd.cc2p1bz2.